Scilight

New Energy Materials and Devices
https://www.sciltp.com/journals/nemd

Article

Effects of Single-Element Doping on the Structural Evolution and High-Voltage Performance of O2-Type $LiCoO_2$

Yilong Han [1], Jintao Zhang [2,*] and Sheng Liu [1,*]

[1] School of Materials Science and Engineering, Nankai University, Tianjin 300350, China
[2] Institute of Materials Research and Engineering (IMRE), Agency for Science, Technology and Research (A*STAR), Singapore 138634, Singapore
* Correspondence: jintao_zhang@imre.a-star.edu.sg (J.Z.); shengliu@nankai.edu.cn (S.L.)

How To Cite: Han, Y.; Zhang, J.; Liu, S. Effects of Single-Element Doping on the Structural Evolution and High-Voltage Performance of O2-Type $LiCoO_2$. *New Energy Materials and Devices* **2026**, *1*(1), 100–110.

Received: 2 July 2026
Revised: 7 August 2026
Accepted: 28 August 2026
Published: 15 September 2026

Abstract: O2-type lithium cobalt oxide ($LiCoO_2$, O2-LCO), featuring a unique ABAC oxygen stacking sequence and enhanced structural reversibility at high voltages, has garnered significant attention in recent years. However, its structural stability and interfacial compatibility during long-term cycling under high-voltage operation remain critical challenges. In this work, Al-, Mg-, Nb-, and B-doped O2-LCO cathode materials with the nominal composition ($LiCo_{0.99}M_{0.01}O_2$, M = Al, Mg, Nb, B) were synthesized via an ion-exchange method. The effects of different dopants on crystal structure, phase-transition behavior, and electrochemical performance of O2-LCO were systematically investigated. The results demonstrate that dopants play critical roles in regulating the structural evolution and cycling stability of O2-LCO. This comparative study provides fundamental insights into dopant-dependent structural evolution and offers guidance for the rational design of high-voltage, high-energy-density layered cathode materials.

Keywords: lithium-ion batteries; O2-type $LiCoO_2$; element doping; structural evolution; cycling stability

1. Introduction

The rapid growth of portable electronics, electric vehicles (EVs), and grid-scale energy storage systems has created an increasing demand for lithium-ion batteries (LIBs) with higher energy densities [1]. Among various cathode materials, lithium cobalt oxide ($LiCoO_2$, LCO) remains one of the most important commercial materials owing to its exceptional tap density and outstanding volumetric energy density [2]. Since Goodenough first reported its electrochemical characteristics in 1980 [3], continuous efforts have been devoted to increasing its operational voltage and specific capacity. To date, commercial LCO can deliver reversible capacities exceeding 190 mAh g^{-1} when charged to 4.55 V (vs. Li/Li^+) [4]. However, conventional O3-type $LiCoO_2$ encounters severe capacity fading and structural degradation when charged to 4.6 V or higher for high capacity, which significantly limits the application of conventional O3-type $LiCoO_2$ [5,6]. O3-type $LiCoO_2$ possesses a rhombohedral layered structure with oxygen atoms arranged in an ABCABC close-packed sequence, where lithium ions occupy octahedral interstitials. Upon deep delithiation ($x < 0.3$ in Li_xCoO_2), the O3 lattice undergoes irreversible interlayer gliding, triggering phase transition toward the H1–3 or even O1 phase [7–9]. These phase transitions are accompanied by pronounced anisotropic lattice strain and volume changes [5,10]. The resulting mechanical stress promotes the initiation and propagation of intragranular cracks, ultimately leading to chemomechanical degradation of the electrode [11]. In addition, the highly oxidizing Co^{4+} species generated at elevated potentials accelerate parasitic side reactions with the electrolyte. This interfacial instability is often compounded by the participation of lattice oxygen in charge-compensation process, which can trigger oxygen release and the formation

of electrochemically inactive Co_3O_4 spinel/rock-salt phase [12]. Collectively, these structural and interfacial degradation processes severely curtail the operational viability of O3-type $LiCoO_2$ in the high-voltage regime.

In contrast to O3-type $LiCoO_2$, O2-type $LiCoO_2$ manifests a unique ABAC oxygen stacking sequence and exists as a thermodynamically metastable phase. Since Delmas et al. first synthesized O2-LCO via an ion-exchange protocol from P2-type $Na_{0.7}CoO_2$ in 1982 [13], researchers have gradually unraveled its idiosyncratic phase transformation kinetics during delithiation. Unlike the O3 variant, O2-LCO transitions into a T2 phase rather than O1 phase under deep delithiation regimes, thereby exhibiting markedly enhanced structural reversibility. Recently, Zan et al. demonstrated that O2-LCO exhibits substantially better cycling stability and rate capability than O3-LCO with comparable particle morphology when operated above 4.5 V (vs. Li/Li^+) [14]. Combined experimental and computational analyses revealed that the superior high-voltage performance originates from faster Li-ion transport, lower diffusion barriers, more homogeneous Li distribution, and enhanced mechanical stability. As a result, stress accumulation within particles is significantly mitigated, thereby suppressing crack formation and improving structural durability during cycling.

Despite its superior structural reversibility, O2-LCO remains thermodynamically metastable and can still suffer from structural degradation and interfacial instability during prolonged high-voltage cycling. These issues continue to limit its long-term electrochemical performance. Therefore, rational structural engineering strategies, particularly elemental doping, are highly desirable to further improve the stability of O2-LCO. Elemental doping is one of the most effective approaches for improving the performance of layered oxide cathodes and has been widely employed in O3-type $LiCoO_2$ [15]. Previous studies have demonstrated that suitable dopants can stabilize the crystal structure, suppress unfavorable phase transitions, mitigate transition-metal dissolution, and enhance lattice oxygen stability, thereby improving cycling durability and high-voltage performance [11,16–19]. Moreover, dopant incorporation can modify the local electronic structure and defect chemistry of $LiCoO_2$, leading to further improvements in electrochemical behavior [12,20]. These strategies provide valuable guidance for the development of high-performance O2-type $LiCoO_2$ cathodes.

Although doping modification of O2-type $LiCoO_2$ has recently attracted increasing attention, the relationships among dopant chemistry, site occupancy, structural evolution, and electrochemical performance remain poorly understood. Owing to the unique ABAC oxygen stacking sequence, O2-LCO exhibits a Li-ion diffusion environment different from that of O3-LCO. Notably, approximately half of the intermediate tetrahedral sites in O2-LCO do not share faces with CoO_6 octahedra, resulting in lower Li-ion migration barriers and faster diffusion kinetics [14]. Thus, the effects of elemental doping in O2-LCO may differ substantially from those established for O3-type $LiCoO_2$. However, a systematic understanding of how different dopants influence the crystal structure, phase-transition behavior, and electrochemical stability of O2-LCO is still lacking.

In this work, a comparative study of four representative dopants, including aluminum (Al), magnesium (Mg), niobium (Nb), and boron (B), was carried out in O2-type $LiCoO_2$. The selection of Al, Mg, Nb, and B was designed to represent distinct chemical characteristics and structural regulation strategies in layered oxide cathodes. Al was selected as a typical electrochemically inactive dopant with strong Al–O bonding capability, which may enhance lattice stability and suppress structural degradation. Mg represents a divalent cation dopant with a relatively larger ionic radius, and its incorporation has been widely associated with a pillar effect that stabilizes layered frameworks. Nb was chosen as a high-valence dopant with a larger ionic size, which can introduce stronger electronic modulation and lattice distortion effects, thereby influencing phase evolution behavior. In contrast, B represents a non-metal dopant with strong B–O bonding affinity and a much smaller ionic radius, providing an opportunity to investigate the effects of local bonding modification and defect chemistry regulation. Therefore, these four dopants provide a broad chemical spectrum for understanding the relationship between dopant characteristics, structural evolution, and electrochemical behavior in O2-type $LiCoO_2$. Their effects on crystal structure, phase-transition evolution, and high-voltage electrochemical performance were systematically evaluated. Through combined X-ray diffraction (XRD) analysis and electrochemical characterization, the structural effects and possible incorporation behaviors of these disparate dopants within the O2-LCO framework were investigated. The results provide valuable insights into dopant-dependent structural evolution and offer guidance for the development of high-performance O2-type layered cathodes for high-voltage lithium-ion batteries.

2. Experimental

2.1. Material Preparation

Pristine O2-type $LiCoO_2$ (LCO) and the doped counterparts, denoted as O2-LCAlO, O2-LCMgO, O2-LCNbO, and O2-LCBO (corresponding to the nominal compositions $LiCo_{0.99}M_{0.01}O_2$ where M = Al, Mg, Nb, B), were synthesized via an ion-exchange protocol from P2-type $Na_{0.7}CoO_2$ (NCO) precursors. Initially, stoichiometric

amounts of Co_3O_4, Na_2CO_3, and respective dopant precursors—namely $Al(OH)_3$, $Mg(CH_3COO)_2{\cdot}4H_2O$, Nb_2O_5, and B_2O_3—were thoroughly homogenized and calcined at 800 °C under a flowing oxygen atmosphere for 48 h to obtain the pristine and doped P2-NCO powders.

For the subsequent ion-exchange process, an aqueous solution with a lithium-ion concentration of 2.5 mol L^{-1} was prepared by dissolving LiCl and $LiOH{\cdot}H_2O$ in deionized water. The as-prepared P2-type precursors (pristine $Na_{0.7}CoO_2$ or nominal doped $Na_{0.7}Co_{0.99}M_{0.01}O_2$) were immersed in this solution with a controlled Li/Na molar ratio of 10:1. The ion-exchange reaction was conducted under reflux condensation at 100 °C for 24 h. The resulting precipitates were recovered by filtration, washed three times with deionized water to remove residual salts, and subsequently dried at 100 °C. The final products obtained were pristine O2-LCO and the doped variants: O2-LCAlO, O2-LCMgO, O2-LCNbO, and O2-LCBO. O2-LCO was further calcined at 600 °C in an oxygen atmosphere for 12 h to obtain O3-LCO. All synthesized powders were stored in an Ar-filled glove box to prevent potential moisture absorption and surface contamination.

2.2. Materials Characterization

The morphologies and microstructures of both the pristine and cycled cathode materials were examined using field-emission scanning electron microscopy (SEM, JSM-7800F, JEOL, Tokyo, Japan). The crystalline structures of the as-prepared samples were characterized by powder X-ray diffraction (XRD, Rigaku Smart Lab, Rigaku, Tokyo, Japan) utilizing Cu Kα radiation. XRD patterns were collected over a 2θ range of 10–80° with a constant scanning rate of 1° min^{-1}. The actual elemental compositions of the doped samples were measured using the inductively coupled plasma optical emission spectroscopy (ICP-OES, Agilent 5110, Santa Clara, CA, USA). Surface composition analysis of the as-prepared samples was performed using X-ray photoelectron spectroscopy (XPS, Thermo Scientific ESCALAB 250Xi, Waltham, MA, USA).

2.3. Electrochemical Tests

To prepare the working electrodes, the active materials (pristine or doped O2-LCO), conductive carbon (Super P), and polyvinylidene fluoride (PVDF) binder were dispersed in N-methyl-2-pyrrolidone (NMP) at a weight ratio of 80:10:10. The resulting homogeneous slurry was uniformly cast onto an aluminum (Al) foil current collector and dried at 110 °C in a vacuum oven overnight. The typical mass loading of the active material was maintained between 2 and 2.6 mg cm^{-2}.

CR2032-type coin cells were assembled in an argon-filled glovebox (H_2O < 0.1 ppm, O_2 < 0.1 ppm) using lithium metal discs as the counter/reference electrode and Celgard 2400 (Celgard, Charlotte, NC, USA) as the separator. The electrolyte consisted of 1 mol L^{-1} $LiPF_6$ dissolved in a mixture of ethylene carbonate (EC) and dimethyl carbonate (DMC) (3:7 by volume). Galvanostatic charge/discharge tests were performed within a voltage range of 3.0–4.6 V, including two initial activation cycles at 0.1 C and long-term cycling stability assessments at 0.5 C (1 C = 200 mA g^{-1}). The cycled electrodes were carefully disassembled from the cells, washed with DMC to remove residual electrolyte, and dried in an Ar-filled glovebox before SEM characterization.

3. Results and Discussion

The actual elemental compositions of the doped samples were determined by using inductively coupled plasma optical emission spectroscopy (ICP-OES) (Table S1, Supporting Information). The measured Co:Dopant mol ratios were 99.34:0.66, 98.38:1.62, 99.76:0.24, and 99.89:0.11 for O2-LCAlO, O2-LCMgO, O2-LCNbO, and O2-LCBO, respectively, confirming the incorporation of Al, Mg, Nb, and B into the final products. The XRD patterns of conventional O3-LCO, pristine O2-LCO, and the doped samples (O2-LCAlO, O2-LCMgO, O2-LCNbO, and O2-LCBO) are shown in Figure 1a. The diffraction peaks of O2-LCO can be indexed to the characteristic crystallographic planes. Notably, upon Nb-doping, an additional diffraction peak appears at 45.22° (Figure 1b). This peak is close to the (104) reflection of O3-LCO located at 45.28°, suggesting the possible presence of a minor O3-type impurity phase. The appearance of this phase indicates that Nb incorporation may reduce the phase stability of O2-LCO and promote a partial O2-to-O3 structural transformation. In contrast, the XRD patterns of the Al-, Mg-, and B-doped samples remain nearly identical to that of pristine O2-LCO, indicating that these dopants do not significantly disrupt the O2 host lattice. Closer inspection reveals that the (100) and (101)/(004) reflections of all doped samples shift slightly toward lower 2θ values (Figure 1d), suggesting a possible variation in the in-plane interplanar spacing. Different trends are observed for the (002) and (103) reflections (Figure 1c,e). Specifically, Mg doping causes these peaks to shift toward higher 2θ values, whereas Al and B doping lead to shifts toward lower angles. In contrast, Nb doping exhibits negligible shift. The distinct peak shifts observed for Mg-doped system suggest possible anisotropic structural responses after Mg incorporation. Previous

studies have suggested that Mg can occupy both Li and Co sites in layered oxides. Li-site occupancy may exert a pillaring effect that stabilizes the layered structure, whereas Co-site occupancy can induce significant distortion within the transition metal layers owing to the different ionic radius and valence state of Mg^{2+}. As a result, the lattice parameters may evolve anisotropically, leading to expansion along the a-axis and contraction along the c-axis. Although the exact Mg occupation site cannot be directly confirmed in this work, the observed lattice evolution and electrochemical behavior are consistent with previously reported Mg-induced stabilization effects. In the cases of Al and B doping, the overall shift of the characteristic peaks toward lower angles suggests a slight lattice expansion. Although Al and B possess strong oxygen-binding affinities, their incorporation into the O2 host lattice might induce localized structural stress or electronic redistribution that increases the d-spacing. These peak variations suggest that heteroatom incorporation may modify the local Co–O coordination environment and lattice configuration. In particular, the lattice expansion observed for B-doped O2-LCO is noteworthy because the ionic radius of B^{3+} (20 pm) is substantially smaller than that of Co^{3+} (54.5 pm). Such behavior implies that B incorporation may not simply occur through direct substitution at Co sites. Instead, it may induce local structural distortion and electronic redistribution within the lattice, resulting in an overall increase in the average d-spacing. Further characterization is required to clarify the exact incorporation mechanism of B in the O2-LCO structure.

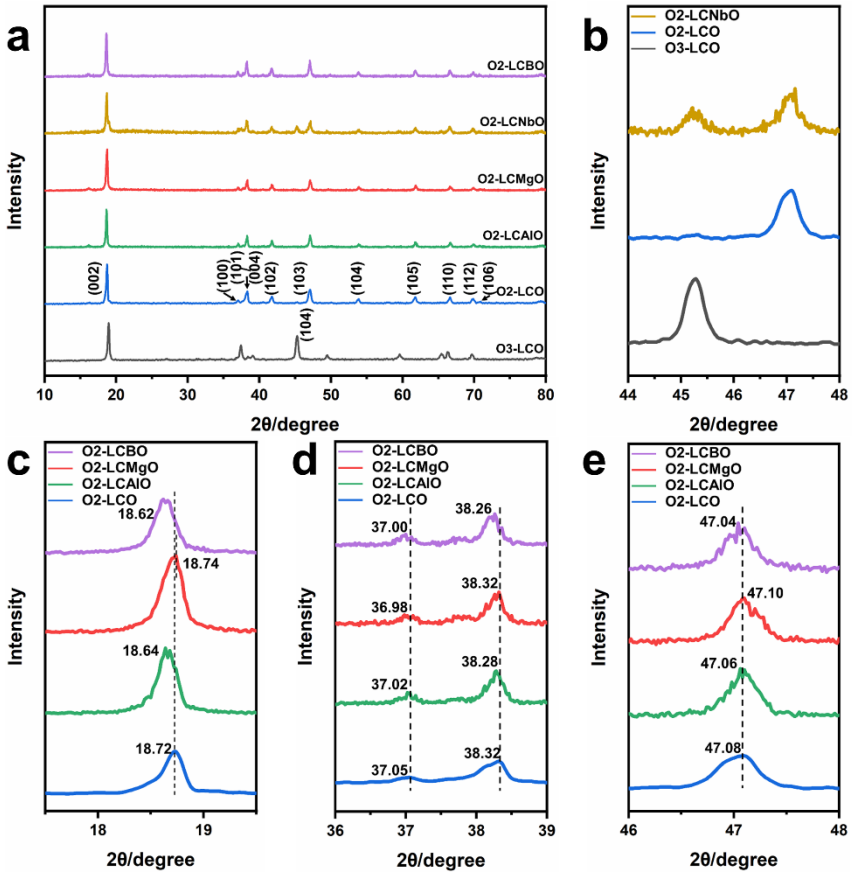

Figure 1. (**a**) XRD patterns of O3-LCO, O2-LCO, and O2-LCO doped with Al, Mg, Nb and B. (**b**) Comparison showing an additional peak in O2-LCNbO corresponding to the (104) reflection of O3-LCO. Representative peak shifts of (**c**) (002), (**d**) (100) and (101)/(004), and (**e**) (103) reflections induced by doping.

The SEM images of pristine and doped O2-LCO materials are displayed in Figure 2. The pristine O2-LCO exhibits an irregular and platelet-like morphology with sharp edges and noticeable surface protrusions. Upon Al and Mg doping, the particles become thinner and display a more pronounced lamellar morphology. In particular, the Al-doped material exhibits a smooth particle surface without noticeable protrusions, suggesting a more uniform crystal growth process. The Mg-doped material shows a similar but less pronounced trend, with some surface asperities still remaining. A significant morphological change is observed in the Nb-doped material. The characteristic platelet-like morphology is partially disrupted and replaced by irregular block-like particles with slightly reduced grain size. This observation is consistent with the XRD results, indicating that Nb incorporation alters the crystal growth behavior and phase stability of O2-LCO. Note that the B-doped material exhibits the most pronounced morphological evolution. The particles become noticeably smaller and tend to adopt a more rounded

morphology. This behavior suggests that B incorporation may influence the nucleation and growth processes during synthesis, leading to suppressed grain growth and modified particle morphology. Such morphology variations may further influence the electrode-electrolyte interfacial area and Li-ion transport characteristics, thereby affecting the electrochemical performance of the doped O2-LCO materials.

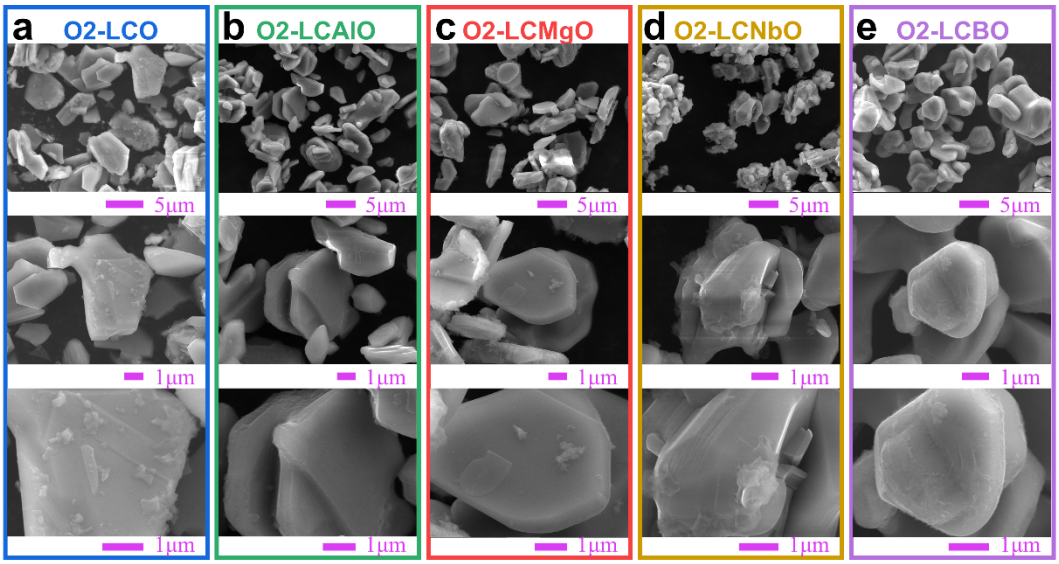

Figure 2. SEM images of (**a**) O2-LCO, (**b**) O2-LCAlO, (**c**) O2-LCMgO, (**d**) O2-LCNbO, and (**e**) O2-LCBO.

The initial charge/discharge profiles of the O3-LCO cathode and the pristine and doped O2-LCO cathodes within the voltage range of 3.0–4.6 V (vs. Li/Li^+) are depicted in Figure S2 (Supporting Information) and Figure 3a–e, respectively. To ensure reproducibility, at least three independent cells were assembled for each composition, and the presented curves in Figure 3a–e are representative ones exhibiting the median discharge capacity among the parallel replicates. The pristine O2-LCO delivers an initial discharge capacity of 208.9 mAh g^{-1}. In comparison, the Al-, Mg-, and B-doped materials show a moderate capacity reduction to 188.1, 202.8, and 192.8 mAh g^{-1}, respectively. The reduced capacity may be related to dopant-induced modifications of the local crystal structure and Li-ion transport environment, which can affect the extent of reversible Li extraction at high voltages. In particular, the incorporation of electrochemically inactive dopants may partially suppress the participation of neighboring Co redox centers, leading to a lower achievable capacity. In contrast, the Nb-doped material exhibits a high discharge capacity of 212.9 mAh g^{-1}. This improvement may be associated with structural changes induced by Nb incorporation, including slight lattice expansion and the formation of a small amount of O3-type phase. These structural features could facilitate Li-ion extraction and increase the degree of delithiation during the initial charge process, thereby contributing to the enhanced discharge capacity.

The underlying mechanisms governing the capacity variations in doped O2-LCO materials can be further elucidated by analyzing the initial Coulombic efficiency (ICE) (Figure 3f). The Al-doped sample exhibits an exceptionally high initial charge capacity (255 mAh g^{-1}) accompanied by a relatively low discharge capacity (188 mAh g^{-1}), resulting in a reduced ICE. To further understand this irreversible capacity loss, XPS measurements were performed on pristine O2-LCO and O2-LCAlO powders (Figure S1, Supporting Information). The O 1s spectra exhibit noticeable differences after Al doping. Specifically, the relative intensity of the high-binding-energy oxygen components located at approximately 531–532 eV increases, whereas the lattice oxygen-related peak near 529 eV decreases. These changes suggest that Al incorporation modifies the surface oxygen chemical environment and increases the contribution of surface oxygen species and defect-related oxygen configurations. Such surface oxygen evolution may promote irreversible interfacial reactions during the initial high-voltage activation process (Figure S3, Supporting Information), contributing to CEI formation and lithium consumption, thereby leading to the reduced initial coulombic efficiency. The Nb-doped sample also delivers a high charge capacity accompanied by a relatively low ICE. This behavior may be related to the structural modifications induced by Nb incorporation. In contrast, Mg-doped O2-LCO exhibits a slight reduction in discharge capacity, which can be attributed to the combined effects of electrochemically inactive Mg species and the enhanced structural stability provided by Mg incorporation. For the B-doped sample, both the charge and discharge capacities decrease compared with those of pristine O2-LCO. Although XRD analysis suggests a slight lattice expansion, the reduced capacity indicates that B incorporation may modify the local bonding environment and Li-ion transport

characteristics, thereby limiting the extent of delithiation. Notably, the B-doped sample exhibits a relatively high ICE, implying reduced irreversible reactions and improved interfacial stability during the initial cycle.

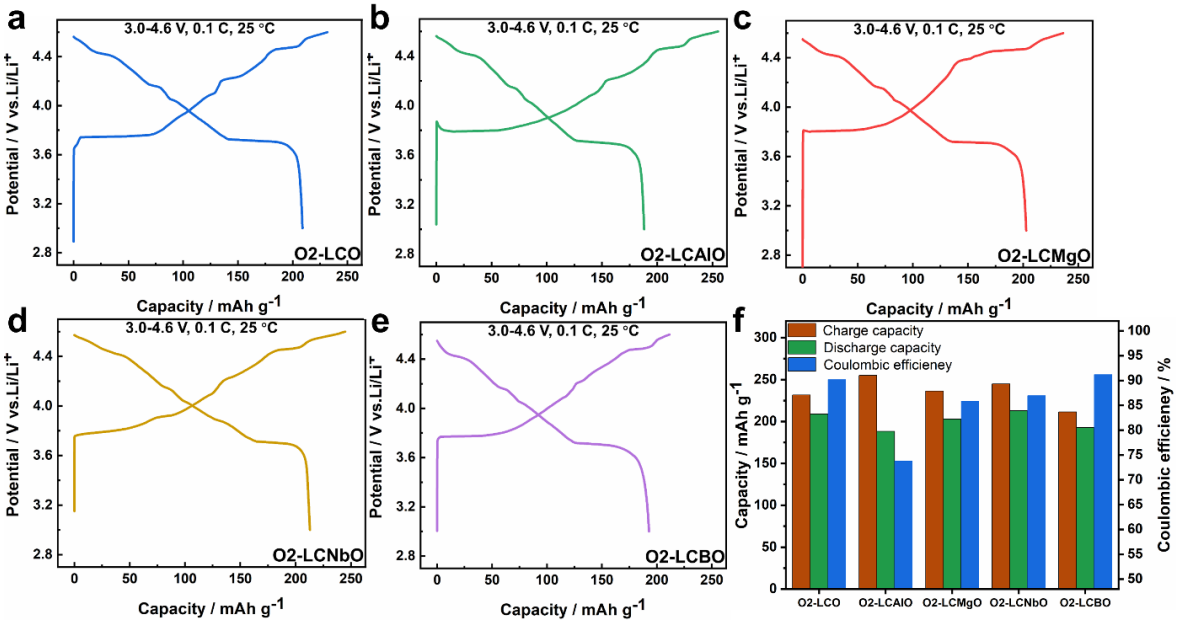

Figure 3. Charge and discharge voltage profiles of (**a**) O2-LCO, (**b**) O2-LCAlO, (**c**) O2-LCMgO, (**d**) O2-LCNbO, and (**e**) O2-LCBO cathodes at 0.1 C-rate between 3.0 and 4.6 V. (**f**) Initial charge-discharge capacity and first-cycle coulombic efficiency of the cathode material before and after doping.

The long-term cycling performance of the pristine and doped O2-LCO electrodes at 0.5 C (1 C = 200 mA g^{-1}) within 3.0–4.6 V is compared in Figure 4a–c. Among all materials, the O2-LCMgO exhibits enhanced capacity retention relative to the pristine O2-LCO. This improvement may be primarily attributed to the "pillaring effect" induced by Mg incorporation, which effectively bolsters the O2 layered framework against structural collapse during deep delithiation. Although the Mg-doped material delivers a slightly lower initial capacity, its slower capacity decay enables it to surpass the pristine material during extended cycling. The Al-doped sample shows no obvious improvement in cycling stability compared with pristine O2-LCO, whereas the Nb-doped sample exhibits a relatively high initial capacity but undergoes accelerated capacity degradation in the later stages of cycling. In contrast, O2-LCBO exhibits a relatively high apparent capacity retention after 300 cycles. However, this value should be interpreted with caution because the capacity retention is affected by its abnormal cycling behavior, including a pronounced initial capacity decay followed by gradual capacity recovery. The unstable Coulombic efficiency evolution (Figure S4, Supporting Information) suggests that B incorporation does not effectively improve the structural reversibility of O2-LCO. The discharge profiles shown in Figure 4d–h further reveal substantial polarization during the early cycling stage. The evolution of Coulombic efficiency and median voltage during cycling is provided in Figures S4 and S5 (Supporting Information). The Mg-doped sample exhibits improved reversibility and voltage retention, whereas the B-doped sample shows substantial fluctuations, consistent with its unstable cycling behavior.

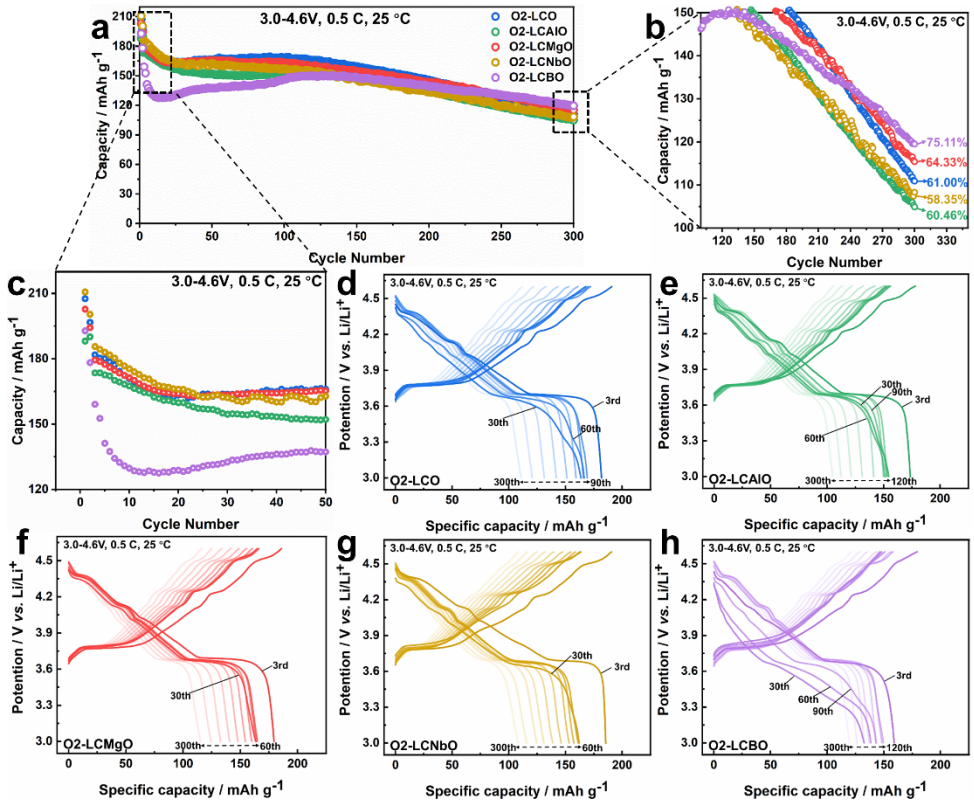

Figure 4. (**a**–**c**) Cycle stability of O2-LCO, O2-LCAlO, O2-LCMgO, O2-LCNbO, and O2-LCBO cathodes at 0.5 C in the range of 3.0–4.6 V. Long-cycle charge-discharge profiles of (**d**) O2-LCO, (**e**) O2-LCAlO, (**f**) O2-LCMgO, (**g**) O2-LCNbO, and (**h**) O2-LCBO within 3.0–4.6 V.

The initial charge/discharge dQ/dV profiles of the O3-LCO, the pristine O2-LCO and the doped samples are displayed in Figure 5, with corresponding phase structures and transition voltages labeled. The O3-LCO profile (Figure 5a) is included as a reference to compare the phase-transition behaviors between conventional O3-type and O2-type $LiCoO_2$. Unlike O2-LCO, O3-LCO exhibits characteristic phase-transition peaks associated with the O3–H1–3 structural evolution during deep delithiation. These irreversible phase transitions are accompanied by significant lattice rearrangement and structural instability, which are considered the primary limitations of O3-LCO under high-voltage operation. In contrast, O2-LCO undergoes a different phase-transition pathway involving the O2–T2 transformation, enabling improved structural reversibility during high-voltage cycling. Notably, the O2-LCAlO electrodes exhibit a unique phenomenon at the onset of charge where the voltage first increases and then decreases (Figure S3, Supporting Information). This behavior is consistently observed in all O2-LCAlO electrodes during the first charging process. This behavior is consistent with the exceptionally high initial charge capacity of O2-LCAlO. Combined with the XPS results, the increased contribution of high-binding-energy oxygen species in O2-LCAlO suggests that Al doping modifies the surface oxygen environment, which may induce additional irreversible surface reactions during the initial charging process. These reactions could contribute to the formation of surface interphase species and partial lithium consumption, resulting in the observed high charge capacity and reduced initial coulombic efficiency. In the initial discharge region of the dQ/dV curves, several data points affected by transient side reactions were excluded from the calculation. The adjacent reliable dQ/dV data were retained, and the missing region was connected using dashed lines only for visual continuity, without affecting the determination of phase-transition positions. More importantly, Al doping slightly delays the O2–T2 phase transition during both charge and discharge processes. Such a shift indicates enhanced phase-transition stability and may contribute to the improved voltage retention observed during cycling. For the Mg-doped cathode, a significant delay in the T2–O6 phase transition during charging is observed, which shifts from approximately 4.2 V in the pristine O2-LCO to nearly 4.4 V. This result demonstrates that Mg incorporation suppresses high-voltage phase transitions during deep delithiation, thereby contributing to the improved cycling stability of O2-LCMgO. Nb-doping presents a distinctive phase-transition behavior. Consistent with the XRD results, an additional dQ/dV peak appears near 3.9 V, which is absent in other electrodes. This peak corresponds to the O3 to monoclinic phase transition characteristic of O3-type $LiCoO_2$ (Figure 5a), providing electrochemical evidence for the presence of an O3-type impurity phase in O2-LCNbO. The coexistence of O2 and O3 phases may contribute to the higher initial capacity of the Nb-doped sample, but it also introduces additional structural instability during

prolonged cycling. In contrast, B doping exerts only a minor influence on the phase-transition sequence during the initial cycle. The O2–T2 transition during charging is delayed by only ~0.03 V, while other changes are negligible. This observation can be attributed to the incorporation of B ions (20 pm) with a smaller ionic radius as compared to Co^{3+} ions (54.5 pm) does not severely disrupt the original crystal structure. The long-term cycling dQ/dV profiles (Figure S6, Supporting Information) further reveal distinct differences among the doped samples. The Al- and Mg-doped electrodes exhibit smaller peak shifts and lower voltage hysteresis during cycling, indicating improved structural reversibility. In contrast, the Nb- and especially the B-doped samples show more pronounced peak broadening and shifting, suggesting increased polarization and less reversible phase evolution. These characteristics are consistent with their inferior cycling stability and larger voltage fluctuations during prolonged operation.

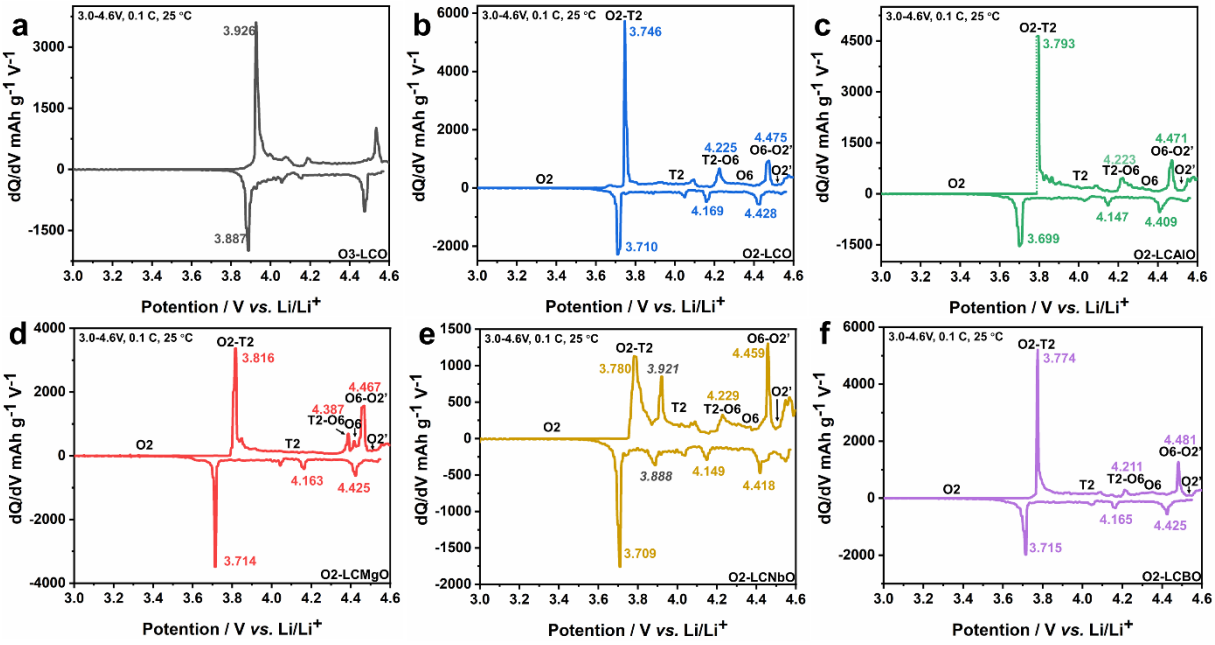

Figure 5. The dQ/dV profiles of (**a**) O3-LCO, (**b**) O2-LCO, (**c**) O2-LCAlO, (**d**) O2-LCMgO, (**e**) O2-LCNbO, and (**f**) O2-LCBO during the initial charge-discharge process.

The post-cycling morphologies of the pristine and doped O2-LCO cathodes after 300 charge/discharge cycles are presented in Figure 6. The Mg-doped cathode exhibits the most well-preserved morphology, with only a limited number of surface microcracks and minimal particle fragmentation. The pristine O2-LCO sample also retains a relatively intact particle structure after cycling. In contrast, the Al-doped material displays obvious surface cracks. More severe structural deterioration is observed in the Nb- and B-doped cathodes, both of which exhibit extensive particle pulverization and widespread fragment dispersion. These morphological observations are consistent with the electrochemical results discussed above. In general, increased particle fragmentation correlates with poorer capacity retention, highlighting the importance of maintaining structural integrity during prolonged cycling. The superior cycling stability of O2-LCMgO relates to its enhanced resistance to crack formation and particle degradation. Conversely, the extensive fragmentation observed in O2-LCNbO is consistent with the structural instability introduced by the O3-type impurity phase identified by XRD and dQ/dV analyses. A distinctive feature is observed in the B-doped sample, where bubble-like surface structures appear in the vicinity of fractured particles after cycling. Such features are absent in the other cathodes. Interestingly, O2-LCBO also exhibits unusual electrochemical behavior, characterized by a rapid initial capacity decay followed by gradual capacity recovery. Although the origin of these bubble-like structures remains unclear, their appearance suggests that B doping may alter the interfacial evolution process during cycling. The coexistence of severe particle fragmentation, abnormal Coulombic efficiency evolution, and unstable cycling behavior indicates that B incorporation introduces additional degradation mechanisms that differ from those observed in the metallic dopant systems.

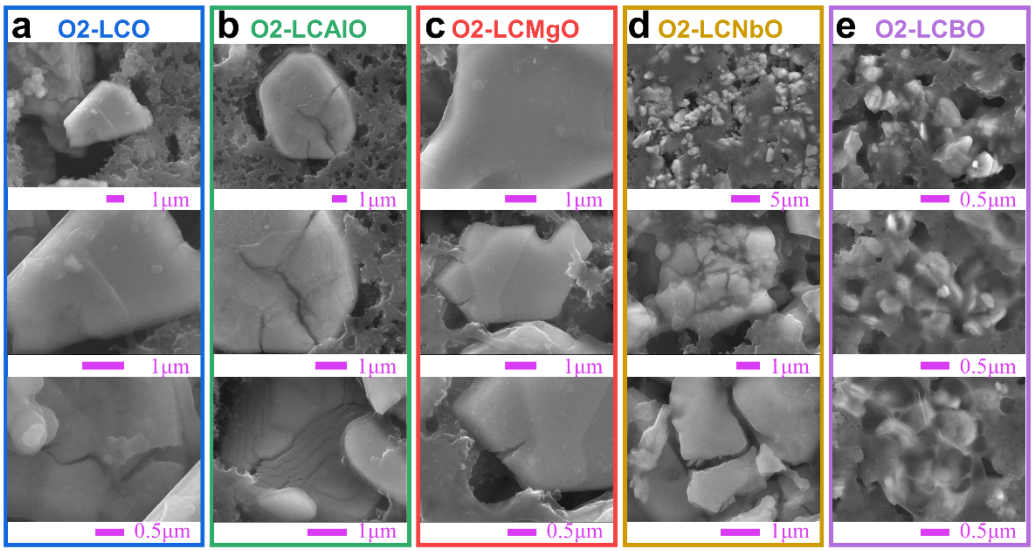

Figure 6. SEM images of the (**a**) O2-LCO, (**b**) O2-LCAlO, (**c**) O2-LCMgO, (**d**) O2-LCNbO, and (**e**) O2-LCBO cathodes after 300 cycles.

On the basis of the above analyses, the effects of different dopants on the structural evolution and electrochemical performance of O2-type $LiCoO_2$ were systematically compared. As summarized in the radar plot shown in Figure 7, each dopant exerts a unique influence on the cathode behavior. Al doping delays phase transitions and improves voltage retention during cycling, indicating enhanced structural stability. It also increases the initial charge capacity; however, the resulting electrochemical benefits are offset by inferior cycling stability, suggesting the presence of irreversible interfacial processes during the initial cycles. Mg doping effectively suppresses high-voltage phase transitions and enhances the structural robustness of the O2 framework, resulting in the best overall cycling stability and capacity retention. Nb doping increases the initial charge/discharge capacities and maintains a relatively high average Coulombic efficiency. However, Nb incorporation also induces the formation of an O3-type impurity phase, which compromises long-term structural stability and ultimately leads to accelerated capacity fading. B doping exhibits the most distinctive behavior. The B-doped cathode shows severe initial capacity decay, unstable Coulombic-efficiency evolution, and extensive particle fragmentation after prolonged cycling. Although the capacity gradually recovers during subsequent cycling, the observed bubble-like surface features and abnormal electrochemical behavior suggest that B incorporation modifies the structural and interfacial evolution pathways of O2-LCO. These results highlight the complex structure-property relationships in O2-type $LiCoO_2$ and demonstrate that achieving optimal electrochemical performance requires balancing phase stability, interfacial compatibility, and reversible lithium-storage capability.

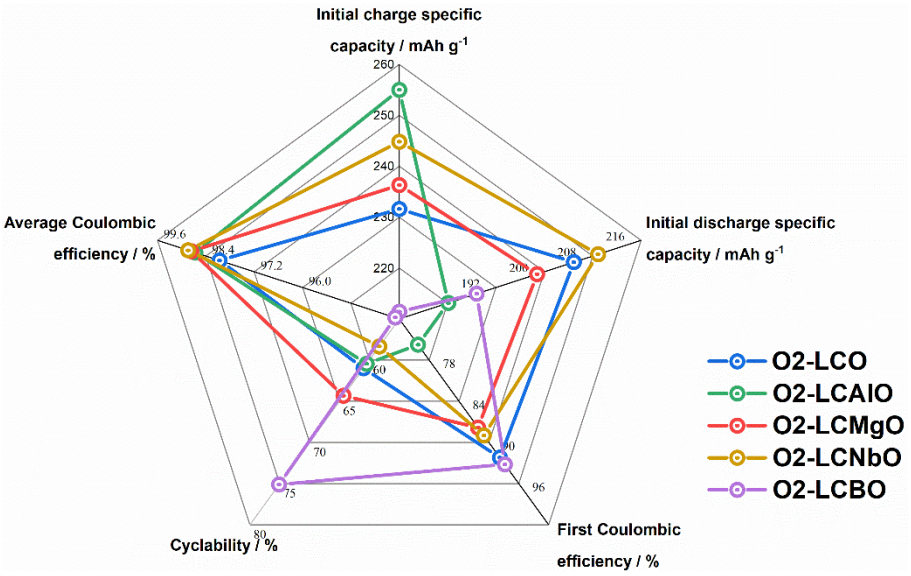

Figure 7. Radar summary chart displaying the comparison of O2-LCO, O2-LCAlO, O2-LCMgO, O2-LCNbO, and O2-LCBO materials.

4. Conclusions

In this work, pristine and single-element-doped O2-type $LiCoO_2$ cathodes (Al-, Mg-, Nb-, and B-doped) were successfully synthesized and systematically evaluated. The results demonstrate that different dopants exert distinct influences on the crystal structure, phase-transition behavior, and electrochemical performance of O2-LCO. Al doping improves phase-transition stability by suppressing phase transitions, whereas Mg doping enhances the overall structural stability and cycling performance. Nb doping increases the initial capacity at the expense of long-term stability due to the formation of an O3-type impurity phase. B doping exhibits a unique degradation behavior during cycling. Among the investigated dopants, Mg delivers the most favorable overall electrochemical performance. This study provides new insights into dopant-dependent structure–property relationships in O2-LCO and offers guidance for the development of high-voltage O2-type cathode materials.

Supplementary Materials

The additional data and information can be downloaded at: https://media.sciltp.com/articles/others/260915100325517 6/NEMD-26070022-SI.pdf. Figure S1: XPS spectra of pristine (**a**) O2-LCO and (**b**) O2-LCAlO. Figure S2: Charge and discharge voltage profiles of O3-LCO cathodes at 0.1 C-rate between 3.0 and 4.6 V. Figure S3: In the early stages of charge, the O2-LCAlO electrode sample exhibited a phenomenon in which the voltage first increased and then decreased. Figure S4: Comparison of Coulombic Efficiency between O2-LCO and (**a**) O2-LCAlO, (**b**) O2-LCMgO, (**c**) O2-LCNbO, (**d**) O2-LCBO cathodes at 0.5C in the range of 3.0–4.6 V. Figure S5: The charge/discharge median voltage evolution of O2-LCO and (**a**) O2-LCAlO, (**b**) O2-LCMgO, (**c**) O2-LCNbO, (**d**) O2-LCBO cathodes at different cycles. Figure S6: The dQ/dV profiles of (**a**) O2-LCO, (**b**) O2-LCAlO, (**c**) O2-LCMgO, (**d**) O2-LCNbO, and (**e**) O2-LCBO cathodes during 300 cycles within 3.0–4.6 V. Table S1: ICP-OES determined elemental composition of the O2-LCAlO, O2-LCMgO, O2-LCNbO, and O2-LCBO cathode.

Author Contributions

Y.H.: Methodology, experiment, data curation, writing—original draft preparation; J.Z.: Conceptualization, writing—reviewing and editing, funding acquisition; S.L.: Supervision, conceptualization, writing—reviewing and editing, funding acquisition. All authors have read and agreed to the published version of the manuscript.

Funding

This work was supported by the National Natural Science Foundation of China (U24A20500).

Institutional Review Board Statement

Not applicable.

Informed Consent Statement

Not applicable.

Data Availability Statement

Data will be made available on request.

Conflicts of Interest

The authors declare no conflict of interest.

Use of AI and AI-Assisted Technologies

During the preparation of this work, the authors used ChatGPT to assist in translating the original Chinese draft into English. After using this tool, the authors reviewed and edited the content as needed and take full responsibility for the content of the published article.

References

1. Ma, X.; Wang, J.; Wang, Z.; et al. Engineering strategies for high-voltage $LiCoO_2$ based high-energy Li-ion batteries. *Electron* **2024**, *2*, e33.

2. Mao, G.Q.; Lu, J.F.; Cai, H.Y.; et al. Optimizing the electrochemical performance of $LiCoO_2$ at 4.5 V via synergistic modification of Mg^{2+} ion doping and $Li_{1.3}La_{0.3}Ti_{1.7}(PO_4)_3$ coating. *Adv. Compos. Hybrid Mater.* **2025**, *8*, 286.
3. Mizushima, K.; Jones, P.C.; Wiseman, P.J.; et al. Li_xCoO_2 ($0 < x < 1$): A new cathode material for batteries of high energy density. *Mater. Res. Bull.* **1980**, *15*, 783–789.
4. Wang, L.L.; Chen, B.B.; Ma, J.; et al. Reviving lithium cobalt oxide-based lithium secondary batteries toward a higher energy density. *Chem. Soc. Rev.* **2018**, *47*, 6505–6602.
5. Lin, Z.Z.; Ying, Y.R.; Li, H.X.; et al. Decoding High-voltage $LiCoO_2$: From Degradation to Stabilization Toward Durable Li-ion Batteries. *Adv. Mater.* **2026**, *38*, e23570.
6. Tan, X.H.; Zhang, Y.X.; Xu, S.Y.; et al. High-Entropy Surface Complex Stabilized $LiCoO_2$ Cathode. *Adv. Energy Mater.* **2023**, *13*, 2300147.
7. Carlier, D.; Van der Ven, A.; Delmas, C.; et al. First-principles investigation of phase stability in the O2-$LiCoO_2$ system. *Chem. Mater.* **2003**, *15*, 2651–2660.
8. Van der Ven, A.; Aydinol, M.K.; Ceder, G.; et al. First-principles investigation of phase stability in Li_xCoO_2. *Phys. Rev. B* **1998**, *58*, 2975–2987.
9. Lu, G.Z.; Lv, J.X.; Wu, X.; et al. Combining Multiple-Element Doping of $LiCoO_2$ and Bilayer Electrolytes for 4.6 V High-Voltage All-Solid-State Lithium Batteries. *J. Phys. Chem. Lett.* **2025**, *16*, 2950–2956.
10. Lin, Z.Z.; Ren, Y.H.; Zhang, C.; et al. Grain boundary engineering enables stable high-voltage $LiCoO_2$ cathodes. *Tungsten* **2026**, *8*, 366–376.
11. Zhang, S.D.; Wang, J.; Grundish, N.S.; et al. High voltage stable $LiCoO_2$ enabled by surface strengthening and bulk doping. *Mater. Today* **2025**, *86*, 238–246.
12. Zhang, J.N.; Li, Q.H.; Ouyang, C.Y.; et al. Trace doping of multiple elements enables stable battery cycling of $LiCoO_2$ at 4.6 V. *Nat. Energy* **2019**, *4*, 594–603.
13. Delmas, C.; Braconnier, J.J.; Hagenmuller, P. A new variety of $LiCoO_2$ with an unusual oxygen packing obtained by exchange reaction. *Mater. Res. Bull.* **1982**, *17*, 117–123.
14. Zan, M.; Xie, H.; Jiao, S.; et al. On the Much-Improved High-Voltage Cycling Performance of $LiCoO_2$ by Phase Alteration from O3 to O2 Structure. *Small Sci.* **2024**, *4*, 2400162.
15. Fang, M.; Yao, Y.T.; Pang, C.; et al. Machine Learning-Assisted Design of Doping Strategies for High-Voltage $LiCoO_2$: A Data-Driven Approach. *Batteries* **2025**, *11*, 100.
16. Song, S.C.; Li, Y.W.; Yang, K.; et al. Interplay between multiple doping elements in high-voltage $LiCoO_2$. *J. Mater. Chem. A* **2021**, *9*, 5702–5710.
17. An, M.; Son, Y. The Critical Roles of Elements in Doping and Coating Strategies for High-Voltage $LiCoO_2$. In *Electrochemical Society Meeting Abstracts 247*; The Electrochemical Society, Inc.: Pennington, NJ, USA, 2025; p. 401.
18. Zhang, P.; Xie, C.; Han, G.; et al. Stable cycling of $LiCoO_2$ at 4.55 V enabled by combined Mg doping and surface coating of NASICON-type electrolyte. *Mater. Today Nano* **2021**, *15*, 100122.
19. Cao, J.; Chen, Z.; Zhong, R.; et al. Study on the Performance of Different Valence Cations Doped into $LiCoO_2$ Cathode for Li-Ion Batteries. *J. Electron. Mater.* **2021**, *50*, 6386–6391.
20. Hoang, K. First-principles theory of doping in layered oxide electrode materials. *Phys. Rev. Mater.* **2017**, *1*, 075403.